High-Fidelity Magnonic Gates for Surface Spin Waves

Xi-guang Wang,[1,*] L. Chotorlishvili,[2] Guang-hua Guo,[1] and J. Berakdar[2]

[1]*School of Physics and Electronics, Central South University, Changsha 410083, China*
[2]*Institut für Physik, Martin-Luther Universität Halle-Wittenberg, Halle/Saale 06099, Germany*

We study the propagation of surface spin waves in two waveguides coupled through the dipole-dipole interaction. Essential for the observations made here is the magnetoelectric coupling between the spin waves and the effective ferroelectric polarization. This allows an external electric field to act on the spin waves and to modify the band gaps of magnonic excitations in individual layers. By on-off switching of the electric field and/or varying its strength or direction with respect to the equilibrium magnetization, it is possible to permit or prevent the propagation of spin waves in a selected waveguide. We propose an experimentally feasible nanoscale device operating as a high-fidelity surface-wave magnonic gate.

I. INTRODUCTION

Magnetostatic surface waves (MSSWs) [1–9] are key elements in magnonic-based information transfer and processing. For realizing efficient magnonic circuits, reliable coupled MSSW waveguides are essential, as they serve as information channels or signal splitters [10,11]. In the present paper, we propose a scheme using electric-field-controlled coupled MSSWs. Microscopically, the mechanism is driven by spin-orbit coupling, which leads to the emergence of a spin-driven electric polarization coupled to spin noncollinearity, as discussed for example for yttrium iron garnet (YIG) [12,13]. The mechanism can be viewed as a dynamical Dzyaloshinskii-Moriya (DM) coupling, and will be referred to as such hereafter. Thus, an external electric field that affects the electric polarization steers the spin order indirectly. In this paper, we focus on YIG as it has a low magnetic damping constant, meaning magnetic losses are negligible on relatively short time scales [14]. A remarkable property of MSSWs is their chiral nature. The chiral character of MSSWs is a purely dynamical effect related to the off-diagonal part of the dynamic dipole-dipole interaction. The dynamically induced chirality leads to at least two exciting phenomena: the nonreciprocal localization of MSSWs propagating perpendicular to the magnetization direction in an in-plane-magnetized thin film, and (b) the prevention of backscattering, i.e., robust spin-wave modes with their frequency located inside the volume-mode (VM) gap; see Refs. [15–18] and references therein. In the present paper, we study the influence of the dynamical DM interaction on the backscattering-immune frequency region in

a single MSSW and in coupled waveguides which are coupled via the dipole-dipole interaction. We show that the nonreciprocal localization of MSSWs in the coupled waveguides leads to nonreciprocal spin-wave (SW) dispersion. Through the DM-interaction term, an electric field influences the dispersion relations of the MSSWs and changes the backscattering-immune frequency region. Furthermore, we study the transfer of MSSWs between two coupled waveguides.

II. THEORETICAL MODEL

To study the effect of an applied external electric field on the excitation and propagation of MSSWs in a thin YIG film, we start from the Landau-Lifshitz-Gilbert (LLG) equation supplemented by the magnetoelectric coupling term [19,20],

$$\frac{\partial \mathbf{M}}{\partial t} = -\gamma \mathbf{M} \times \left(\mathbf{H}_{\text{eff}} - \frac{1}{\mu_0 M_s} \frac{\delta E_{\text{elec}}}{\delta \mathbf{m}} \right) + \frac{\alpha}{M_s} \mathbf{M} \times \frac{\partial \mathbf{M}}{\partial t}. \tag{1}$$

Here $\mathbf{M} = M_s \mathbf{m}$, M_s is the saturation magnetization, $\mathbf{m}$ is the unit vector along the magnetization direction, γ is the gyromagnetic ratio, $\mu_0 = 4\pi \times 10^{-7} \text{ N/A}^2$ is the permeability, and α is the phenomenological Gilbert damping constant. The effective field $\mathbf{H}_{\text{eff}} = (2A_{\text{ex}}/\mu_0 M_s) \Delta \mathbf{m} + \mathbf{H}_{\text{demag}} + H_0 \mathbf{y}$ consists of the exchange field, the demagnetization field, and the external magnetic field applied along the y axis. A_{ex} is the exchange constant. The magnetoelectric coupling term $E_{\text{elec}} = -\mathbf{E} \cdot \mathbf{P}$ describes the coupling between the spin-driven ferroelectric polarization $\mathbf{P}$ and the applied external electric field $\mathbf{E}$. This ferroelectric polarization of YIG in the continuous limit has the form $\mathbf{P} = c_E[(\mathbf{m} \cdot \nabla)\mathbf{m} - \mathbf{m}(\nabla \cdot \mathbf{m})]$, which makes

_____
*wangxiguang@csu.edu.cn

clear the similarity to the Dzyaloshinskii-Moriya interaction. Microscopically, the macroscopic effective electric polarization is magnetically driven. The dynamic spin noncollinearity results in an effective electric polarization **P**. The driving mechanism is effectively a dynamic DM interaction with a DM-interaction vector $\mathbf{D} = -J(ea/E_{\mathrm{SO}})\mathbf{E} \times \mathbf{e}_{n,n+1}$, as discussed for example in Ref. [13]. Here, $E_{\mathrm{SO}} = \hbar^2/2m_e\lambda^2$, J is the exchange coefficient, m_e is the mass of the electron, e is the electron charge, λ is the spin-orbital coupling constant, and $\mathbf{e}_{n,n+1}$ is the unit vector connecting the magnetic ions. For the parameters $|\mathbf{E}| = 3.4$ MV/cm, $E_{\mathrm{SO}} = 3.4$ eV ($\lambda = 1$ Å) and $a = 12 \times 10^{-10}$ m, the effective DM-interaction constant scales with the exchange constant $D/J = 0.12$. This estimation is in line with experimental observations in Ref. [12]. The demagnetization field in the presence of the magnetic dipole-dipole interaction reads

$$\mathbf{H}_{\mathrm{demag}}(\mathbf{r}) = -\frac{M_s}{4\pi} \int_V \nabla \nabla' \frac{1}{|\mathbf{r} - \mathbf{r}'|} \mathbf{m}(\mathbf{r}') \, d\mathbf{r}'. \quad (2)$$

In numerical calculations, we adopt the following material parameters for YIG: $M_s = 1.4 \times 10^5$ A/m, $A_{\mathrm{ex}} = 3 \times 10^{-12}$ J/m, damping constant $\alpha = 0.001$, and magnetoelectric coupling $c_E = 0.9$ pC/m. A magnetic field of amplitude $H_0 = 4 \times 10^5$ A/m is applied along the y axis (see for example Fig. 2).

III. SPIN-WAVE DISPERSION

We utilize Eq. (1) and numerically explore the dispersion relation of the MSSWs. Simulations are done for a 20-nm × 10-μm × 20-nm unit simulation cell covering a single film with a size of 30 μm × 10 μm × 80 nm. For the numerical integration of the LLG equation [Eq. (1)], we utilize the Dormand-Prince method (RK45) with a fixed time step of 0.5 ps. To calculate the SWs and dispersion curves, we first let the magnetization relax to the stationary state. Afterwards, we consider the stationary state as the ground state and add the SW excitation on top of the ground state. To excite SWs over a wide frequency range, we utilize a periodic field pulse $h(t) = h_a\mathbf{y}\sin(2\pi f_H t)/(2\pi f_H t)$, with an amplitude $h_a = 1$ T and cutoff frequency $f_H = 25$ GHz, applied locally to the region of the sample $x = 0$. We analyze the fluctuation statistics extracted from each cell M_x during 200 ns of observation with a time step of 20 ps. The frequency resolution of the spectrum obtained is 0.005 GHz. To calculate the SW dispersion relation, we use a two-dimensional fast Fourier transform $M_x(k_x, f) = (1/N)\sum_{i=1}^{N_z} F_2[M_x(x, z_i, t)]$. Here, z_i is the ith cell along the z axis, and N_z is the total number of cells along the z axis. Simulations done for a cell size of 10 nm × 10 μm × 10 nm (not shown) lead to identical results. The local
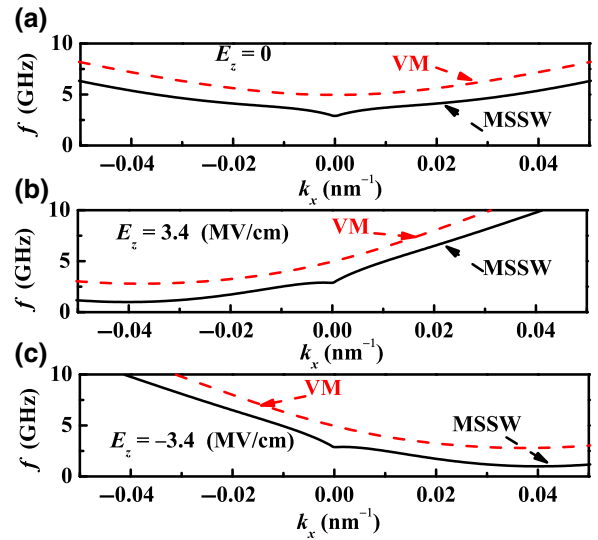

FIG. 1. Spin-wave dispersion relation simulated for a single film in the presence of an electric field $\mathbf{E}_z$ along the z direction with amplitude $E_z = 0$ (a), $E_z = 3.4$ MV/cm (b), and $E_z = -3.4$ MV/cm (c). The MSSWs and volume modes are shown by the black solid lines and red dashed lines, respectively.

equilibrium magnetization is parallel to the y axis, and the MSSW propagates along the x axis.

An applied electric field (along the z axis) causes an asymmetry in the SW dispersion relations of the MSSWs. The results for a single film are shown in Fig. 1. A positive electric field E_z shifts the dispersion relation towards the lower left side, while a negative E_z shifts it towards the lower right side.

The dispersion relation of the MSSW (see Fig. 1) calculated for the single film has a minimum at the point $k_x = 0$. Profiles of the amplitudes of propagating MSSWs are presented in Fig. 2. As we see, the amplitude of a MSSW propagating in the $+x$ direction has a maximum at the upper surface ($z = 80$ nm) (Fig. 2), whereas, in contrast, the amplitude of a MSSW propagating in the reverse direction, $-x$, has a maximum at the lower surface. Reversing the local magnetization switches the upper and lower surfaces (not shown). Thus the localization of the MSSW either in the upper or the lower surface has a chiral character.
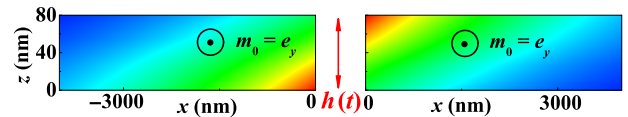

FIG. 2. Spatial profiles of amplitudes of MSSWs propagating in a single film without an electric field ($E_z = 0$). The MSSW is excited at $x = 0$ by the local microwave field $h(t)$. The frequency of the field is equal to 5 GHz.
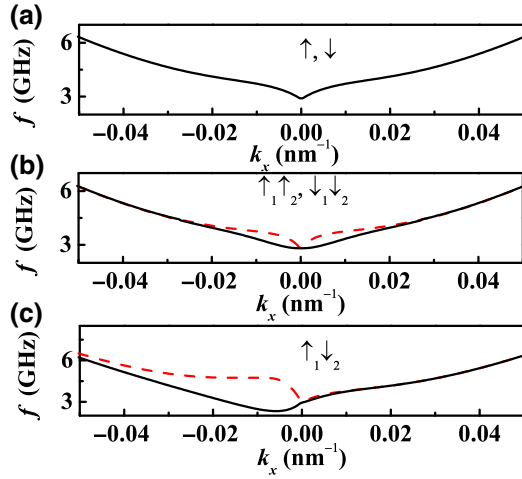
FIG. 3. Simulated spin-wave dispersion relation in (a) a single film (the equilibrium magnetization is oriented along the $+\mathbf{e}_y$ ($\uparrow$) or $-\mathbf{e}_y$ ($\downarrow$) direction), (b) two films with parallel equilibrium magnetizations ($\mathbf{m}_{0,1}$ and $\mathbf{m}_{0,2}$ with both aligned along $\uparrow\uparrow$ or $\downarrow\downarrow$), and (c) two films with antiparallel equilibrium magnetizations ($\mathbf{m}_{0,1} = \uparrow$ and $\mathbf{m}_{0,2} = \downarrow$). If $\mathbf{m}_{0,1} = \downarrow$ and $\mathbf{m}_{0,2} = \uparrow$, i.e., in the case of antiparallel equilibrium magnetization of the films, the dispersion relation is asymmetric with respect to the point $k_x = 0$. The black solid and red dashed curves for the coupled layers represent acoustic and optic surface-wave modes, respectively.

As the next step, we consider two coupled MSSW waveguides and analyze the MSSW dispersion relation for the two coupled waveguides. A spacer of thickness $\sigma = 40$ nm is inserted between two films of the same thickness $t = 80$ nm. The dipolar coupling between the films leads to the formation of "acoustic" and "optic" modes [21,22]. The dispersion relation of the coupled MSSW modes is shown in Fig. 3. When the two films have the same equilibrium magnetization [Fig. 3(b)], the dispersion relations have an axial symmetry with respect to the point $k_x = 0$. In both films, the amplitudes of the MSSWs are stronger at either the upper or the lower surface, depending on the orientation of the equilibrium magnetization and the propagation direction (Fig. 4). For two films with opposite magnetizations [Fig. 3(c)], the dispersion
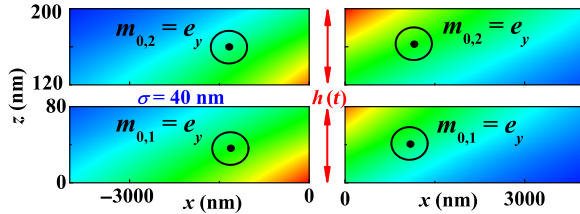

FIG. 4. Spatial profiles of amplitudes of MSSWs propagating in two films with parallel ground-state magnetizations without electric field ($E_z = 0$). The local microwave field $h(t)$ is applied at the edges of both films at $x = 0$. The frequency of the microwave field is equal to 5 GHz.
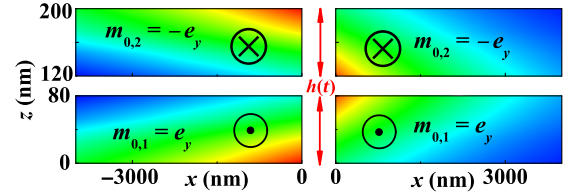

FIG. 5. Spatial profiles of amplitudes of MSSWs propagating in two films with antiparallel ground-state magnetizations. The local microwave field $h(t)$ is applied at the edges of both films at $x = 0$. The frequency of the microwave field is equal to 5 GHz.

relations become rather different and asymmetric. The gap between the two MSSW modes is much larger for MSSWs propagating in the negative ($-x$) direction. Because of the opposite magnetizations, the stronger MSSWs are located at different surfaces in the two films, as is shown in Fig. 5. Switching of the magnetization direction either for a single film or for two parallel films has no impact on the MSSW dispersion relations, while for antiparallel films the dispersion is flipped relative to the point $k_x = 0$. Hence, the MSSW dispersion relation becomes chiral and nonreciprocal when the films are antiparallel.

IV. ANALYTICAL MODEL

We develop a simple analytical model to understand the MSSW dispersion relations for both single and coupled magnetic films. We apply a constant electric field along the z axis $\mathbf{E} = (0, 0, E_z)$, while the static equilibrium magnetization is oriented parallel to the y axis, i.e., $\mathbf{m}_{0,p} = \pm\mathbf{e}_y$. The magnetization vectors in the first and second films ($p = 1, 2$) have the form $\mathbf{m}_p(r, t) = \mathbf{m}_{0,p} + \mathbf{m}_{\mathrm{SW},p} \exp(i(\boldsymbol{\kappa} \cdot \mathbf{r} + \omega t))$. Here, $\mathbf{m}_{\mathrm{SW},p} \ll 1$ is the small deviation of the magnetization from equilibrium. The wave vector $\boldsymbol{\kappa}$ is the sum of the in-plane wave vector $\mathbf{k} = k_x\mathbf{e}_x + k_y\mathbf{e}_y$ and the perpendicular (to the x-y plane) wave vector k_z. We insert the magnetization vector $\mathbf{m}_p(r, t)$ into Eq. (1) and deduce

$$i(\omega - \omega_E)\mathbf{m}_{k,p} = \mathbf{m}_{0,p} \times \sum_q \hat{\boldsymbol{\Omega}}_{pq} \cdot m_{\mathrm{SW},q}. \quad (3)$$

Here, $p, q = 1, 2$ enumerates the layers, and the tensor $\hat{\boldsymbol{\Omega}}_{pq}$ has the form

$$\hat{\boldsymbol{\Omega}}_{pq} = \omega_{\mathrm{ex}}\delta_{pq}\hat{\mathbf{I}} + \omega_M\hat{\mathbf{F}}(d_{pq}). \quad (4)$$

Here, for the sake of brevity, we introduce the following notation: $\omega_{\mathrm{ex}} = \gamma H_0 + a_{\mathrm{ex}}k^2$, $a_{\mathrm{ex}} = 2\gamma A_{\mathrm{ex}}/(\mu_0 M_s)$, $\omega_M = \gamma M_s$, and $\omega_E = 2(\mathbf{m}_{0,p} \cdot \mathbf{e_y})\gamma c_E E_z k_x/(\mu_0 M_s)$. The wave vector k is equal to $\sqrt{k_x^2 + k_y^2}$, the distance between the two waveguides d_{pq} is equal to $t + \sigma$, and σ is the gap between the waveguides. The dynamic magnetodipolar interaction
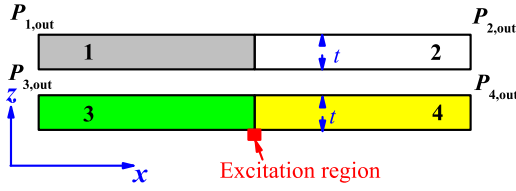
FIG. 6.   Schematic of the dipolar coupled SW waveguide. Two magnetic films lying in the x-y plane are separated by a spacer along the z direction. The SW excitation antenna (red region) is located in the center of the lower magnetic layer. With respect to the center, each magnetic layer is divided into two zones, and the output power of the SWs is detected at four terminals ($P_{i,\text{out}}$).

is described by the tensor [10,23,24] $\hat{\mathbf{F}}$:

$$\hat{\mathbf{F}}(d_{pq}) = \int \hat{\mathbf{N}}(d_{pq})e^{i\mathbf{k}\cdot\mathbf{r}}\frac{d^2\mathbf{k}}{(2\pi)^2},$$

$$\mathbf{N}_{\alpha\beta}(d_{pq}) = \frac{1}{h}\int D_p(k_z)D_q^*(k_z)\frac{\kappa_\alpha\kappa_\beta}{\kappa^2}e^{ik_z d_{pq}}\frac{dk_z}{2\pi}. \tag{5}$$

Here, the "shape amplitude" $D_p(k_z) = \int_{-h_s/2}^{h_s/2} m(z)e^{-ik_z z}dz$ describes the influence of the finite thickness of the thin film. A pictorial plot of the system is shown in Fig. 6. The SW waveguide consists of two thin magnetic films positioned in the x-y plane. The thicknesses of the films are t. In the z, direction the films are separated by a spacer of thickness σ. The distance between the centers of the films is $d_{12} = t + \sigma$. Each film is divided into two regions. The output power of the SW is detected at four ports P_i. The spin wave is excited by an antenna attached to the bottom of the lower film (red region). The MSSWs are mainly located near the upper or lower surface (see Fig. 2). We thus introduce a localization thickness h_s, which is less than the real thickness t. Because of the dipolar coupling at the boundaries, the thicknesses of the MSSW profiles in the two films are identical and pinned together. Therefore, we use the same ansatz $m(z) \sim \cos(k_z^p z)$ to describe the induced nonuniform thickness profiles in both films.

From Eq. (3), we obtain expressions for the dispersion relations of the MSSW modes. The dispersion relation for the MSSW mode in an isolated film reads

$$\omega(\mathbf{k}) = \sqrt{\Omega^{xx}\Omega^{zz}} + \omega_E$$
$$= \sqrt{[\omega_{\text{ex}} + \omega_M F^{xx}(0)][\omega_{\text{ex}} + \omega_M F^{zz}(0)]} + \omega_E. \tag{6}$$

From Eq. (6), we evaluate the difference between the frequencies of counterpropagating spin waves, $\Delta\omega = |\omega(|k_x|) - \omega(-|k_x|)| = 4\gamma c_E E_z k_x/(\mu_0 M_s)$. This result is similar to that obtained in earlier studies [25]. The dispersion relation for two coupled layers with the same local
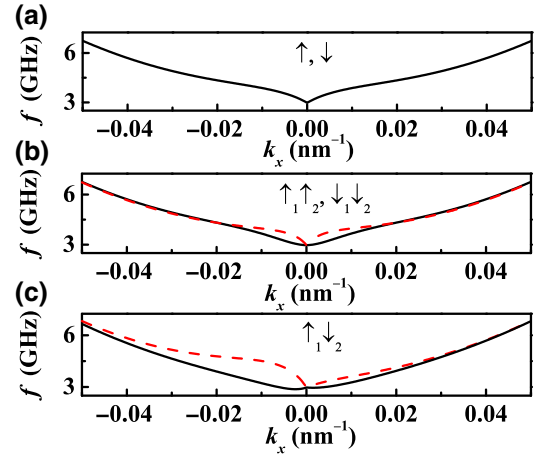

FIG. 7.   Spin-wave dispersion relation, analytical results: (a) a single film (magnetization aligned along the $+\mathbf{e}_y$ (↑) or $-\mathbf{e}_y$ direction (↓)), (b) two parallel coupled films ($\mathbf{m}_{0,1}$ and $\mathbf{m}_{0,2}$; the magnetization in both films is aligned along the ↑↑ or ↓↓ direction), and (c) two coupled films, where the directions of magnetization are antiparallel ($\mathbf{m}_{0,1} = ↑$ and $\mathbf{m}_{0,2} = ↓$).

magnetization is

$$\omega(\mathbf{k}) = \sqrt{[\Omega^{xx} \pm \omega_M F^{xx}(d_{12})][\Omega^{zz} \pm \omega_M F^{zz}(d_{12})]} + \omega_E. \tag{7}$$

If the magnetizations of the layers are opposite to each other, the dispersion relation takes the form

$$\omega(\mathbf{k}) = \{\omega_E^2 + \Omega^{xx}\Omega^{zz} - F^{xx}(d_{12})F^{zz}(d_{12})\omega_M^2$$
$$\pm [4\omega_E^2\Omega^{xx}\Omega^{zz} + \omega_M^2(F^{zz}(d_{12})\Omega^{xx}$$
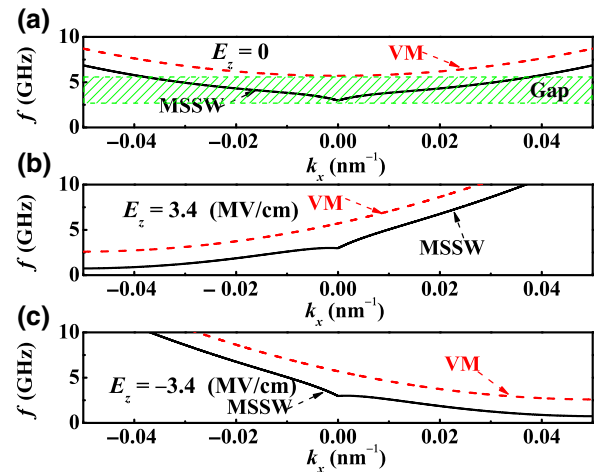$$- F^{xx}(d_{12})\Omega^{zz})^2]^{1/2}\}^{1/2}. \tag{8}$$

FIG. 8.   Analytically obtained spin-wave dispersion relations for an applied electric field $E_z = 0$ (a), $E_z = 3.4$ MV/cm (b), and $E_z = -3.4$ MV/cm (c).
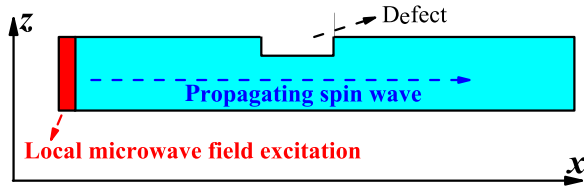
FIG. 9. Pictorial representation of MSSW waveguide with thickness t. The waveguide film is aligned with the x-y plane. A surface defect is embedded in the center of the waveguide. The spin wave propagates along the $+x$ axis and is excited locally at the left edge of the waveguide.

With these analytical expressions, we insert the same material parameters as used in the numerics, and calculate the MSSW dispersion relations. For the profile thickness of the fundamental surface wave, we take $k_z^p = 0$. To simplify the calculation, for a single film and for parallel films we use $h_s = t$. The analytical results for the MSSW dispersion relations plotted in Fig. 7 are in good agreement with the numerical results. In the case of films with antiparallel ground-state magnetizations (see Fig. 5), the thickness of the localized MSSW depends on the propagation direction, and the localization thickness h_s is smaller when the MSSW propagates in the $+x$ direction. Thus, using different values of h_s for different propagation directions, we obtain distinct MSSW dispersions, as shown in Fig. 7(c). Reversing the magnetization in both films reverses the localization thickness h_s of the MSSW propagating in the $+x$ direction, and flips the MSSW dispersion relations. Despite the relative simplicity and approximations, our analytical model and the results obtained are in good agreement with the exact results of the micromagnetic numeric simulation. In both cases, we observe that an applied electric field leads to asymmetric MSSW dispersion relations; see Figs. 1 and 8. The slight quantitative difference between the numeric and analytical results arises due to the approximations made in the analytical model.

V. SPIN-WAVE PROPAGATION IN A WAVEGUIDE WITH A DEFECT

Chiral MSSWs are protected against surface inhomogeneities and defects if the frequency of the MSSW
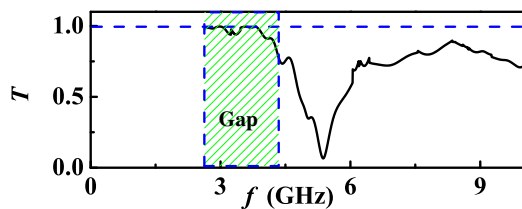

FIG. 10. Transmission ratio T of the MSSW as a function of frequency. The MSSW propagates through the region containing the defect. No electric field is applied ($E_z = 0$). The value $T = 1$ corresponds to perfect transmission.
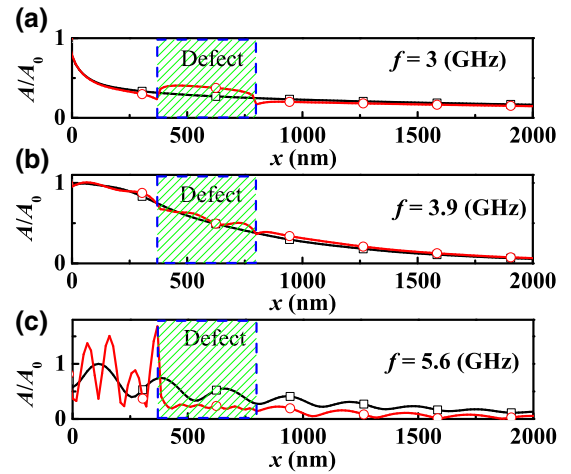

FIG. 11. Spatial distributions of normalized amplitudes $A(x)/A_0$ of excited spin waves along x. The waves are located on the surface of the waveguide. The frequencies f of the waves are (a) 3 GHz, (b) 3.9 GHz, and (c) 5.6 GHz. The amplitude A is normalized to the maximum value A_0 of the line with black squares (when there is no defect), and the line with red circles represents the MSSW amplitude with the defect. The electric field is zero ($E_z = 0$).

matches the band gap [15]. The width of the band gap is quantified in terms of the difference between the minimum threshold frequencies of the VM and the MSSW mode, as demonstrated in Fig. 8(a). Our numerical simulations confirm this result. In the calculation we use a sinc field $h_a \sin(2\pi f_H t)/(2\pi f_H t)\mathbf{y}$, $h_a = 1$ T, and $f_H = 25$ GHz applied locally at the left edge of the waveguide (Fig. 9). Thus, spin waves in the frequency interval $0 < f_H < 25$ GHz are excited. Spin waves with frequencies lower than the smallest frequency of the MSSW mode cannot propagate.

Without an electric field ($\mathbf{E} = 0$), the lower frequency bound of the MSSW is about 2.8 GHz (see Fig. 1). An embedded defect at the surface of the film induces scattering of the spin wave. The scattering process depends strongly on the frequency of the spin wave $f = \omega/(2\pi)$. Comparing the amplitudes of the spin waves in the waveguide with (A_{with}) and without (A_{without}) the embedded defect, we numerically evaluate the transmission ratio T
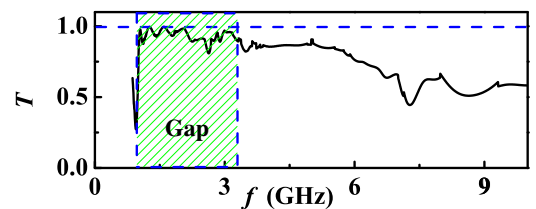

FIG. 12. Transmission ratio T of the MSSW as a function of frequency. The MSSW propagates through the region containing the defect, and $E_z = 3.4$ MV/cm.
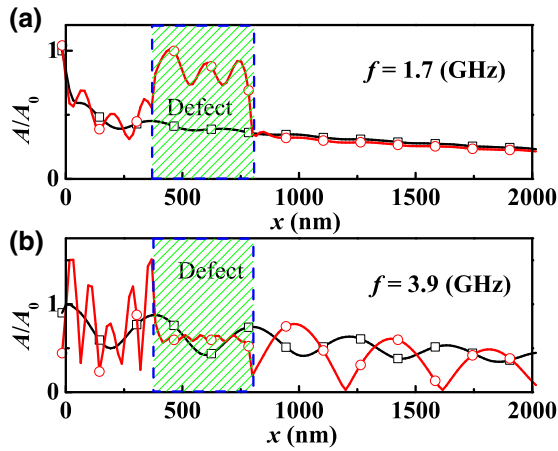
FIG. 13. Spatial distributions of the normalized amplitudes $A(x)$ of spin waves. The waves are located on the surface of the waveguide. The frequencies f of the waves are (a) 1.7 GHz and (b) 3.9 GHz. The applied electric field is $E_z = 3.4$ MV/cm.

and quantify the transmission coefficient of spin waves to describe the scattering process (Fig. 10). In the gap, T is about 1, indicating that the bulk of the MSSWs can be transmitted through the defect without reflection, i.e., backscattering is not permitted. The transmission T becomes much smaller than 1 outside the gap, due to strong reflection from the defect. We also compare the spatial distributions of A_{with} and A_{without} in Fig. 11. In the absence of the embedded defect, the amplitude A decays in the x direction. In addition, at $f = 5.6$ GHz (beyond the gap), due to the interaction between two SWs with different wave vectors (the MSSW and the VM), the amplitude A is not uniform and oscillates with x. After embedding the defect, we see a clear signature of the reflection process and of the scattering from defects for $f = 5.6$ GHz ($T = 0.34$),
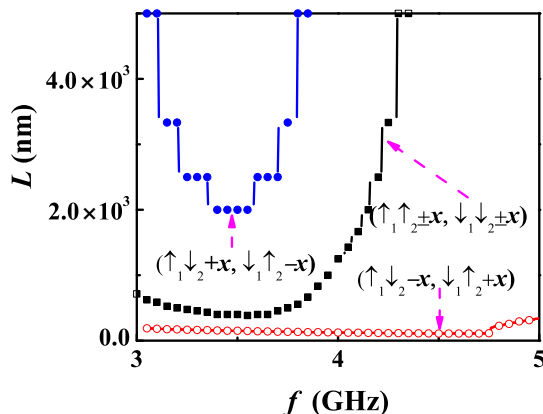

FIG. 14. Coupling length L between spin waves as a function of the spin-wave frequency f. For parallel films, $\uparrow_1\uparrow_2$ or $\downarrow_1\downarrow_2$, L is insensitive to the propagation direction $\pm x$ of the SWs. In the case of antiparallel magnetizations of the films, $\uparrow_1\downarrow_2$ or $\downarrow_1\uparrow_2$, the propagation lengths L of the SWs are different for $+x$ and x.
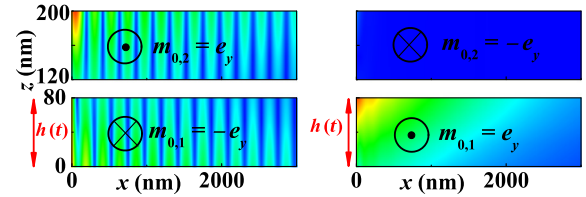

FIG. 15. Spatial profiles of amplitudes of propagating SWs in two antiparallel films at 4.5 GHz. The local microwave field $h(t)$ is applied to the lower film at $x = 0$. Left and right panels correspond to opposite magnetizations.

whereas for $f = 3$ GHz ($T = 1$), the spin wave is entirely transmitted through the defect. Our results are in a good agreement with Ref. [15].

Applying an electric field shifts the gap down and thus decreases the frequency interval in which $T \approx 1$, as shown in Fig. 12. In the frequency interval $1 < f < 3$ GHz, the frequency of the MSSW matches the band gap, and therefore the MSSW can be transmitted through the defect entirely without reflection [as demonstrated by the amplitude $A(x)$ for the frequency $f = 1.7$ GHz ($T = 0.96$) in Fig. 13(a)]. Outside the band gap, the reflection of the spin wave at the defect becomes significant (Fig. 12). The reflection $A(x)$ at $f = 3.9$ GHz ($T = 0.85$) is shown in Fig. 13(b).

VI. SPIN-WAVE TRANSFER BETWEEN TWO COUPLED FILMS: THE ROLE OF THE ELECTRIC FIELD

We consider the dynamics of two simultaneously excited propagating SW modes. The waveguides are coupled through the dipole-dipole interaction. The dipole-dipole coupling splits the waveguide modes into symmetric (acoustic) and asymmetric (optical) modes. The acoustic and optical modes may interact and exchange energy. The transfer of energy takes place on a characteristic length scale $L = \pi/\Delta k_x$, termed the "coupling length" [10]. The coupling length L characterizes the propagation length of the SW excitation in the first waveguide
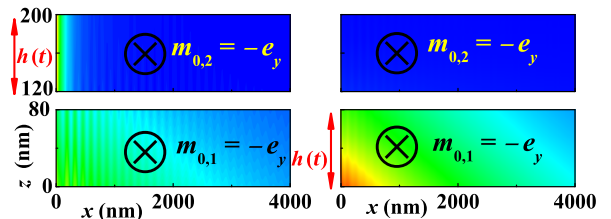

FIG. 16. An electric field $E_z = 3.4$ MV/cm is applied to the bottom layer. The frequency f of the local microwave field applied to the bottom (or top) film at $x = 0$ in the right (or left) panel is 1 GHz. The spatial profiles of the amplitudes of propagating MSSWs are plotted.
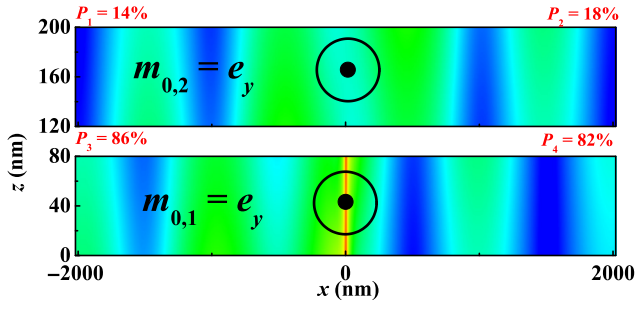
FIG. 17. Spatial profiles of amplitudes of propagating SWs in two parallel films. P_1 and P_3 are located at the left side of the waveguide ($x = -2000$ nm), and P_2 and P_4 are located at the right side. The SWs are excited by a rf field with frequency 3.2 GHz.

before transferring its energy to the second waveguide, i.e., the "mean free path" of the SW. The quantity Δk_x is the difference between the wave vectors of the acoustic and optical modes at the same frequency. The simulated value of the coupling length L depends on the frequency f of the propagating wave; see Fig. 14. Our results show that the coupling length L and the energy transfer process can be controlled through two factors: the direction of the equilibrium magnetization and the direction of propagation of the SWs. For example, for $f = 4.5$ GHz, $L \approx \infty$ for $m_{0,1} = e_y$ and $m_{0,2} = -e_y$ is much larger than $L = 100$ nm for $m_{0,1} = -e_y$ and $m_{0,2} = e_y$. The energy transfer can be switched on and off via switching the magnetization directions. The propagating SW excited in the lower film (Fig. 15) is effectively decoupled from the upper film when $L \approx \infty$. The energy transmission is switched when $L = 100$ nm after reversing the magnetization.

Besides, an electric field shifts the SW dispersion relation in the coupled films, and this fact is important for controlling the transmission properties of the SWs. An electric field $\mathbf{E} = (0, 0, E_z)$ applied only to a single film shifts selectively the dispersion relation solely in that layer (similarly to Fig. 1). Therefore, a SW at a frequency lower than 3 GHz can propagate in the selected film, while propagation in the second layer is forbidden. To illustrate
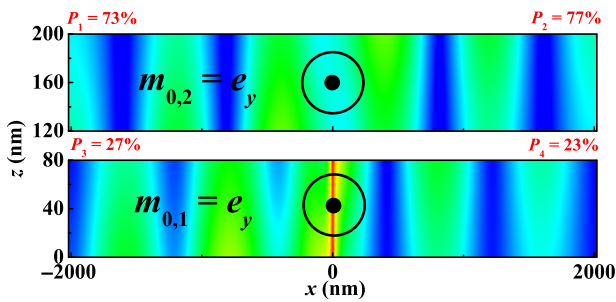
this statement, we apply a microwave field of frequency $f = 1$ GHz to the bottom or top layer in the vicinity of the region $x = 0$ and excite a SW. A constant electric field is applied to the bottom layer only. The SW propagates in the bottom layer, while propagation in the top layer is restricted; see Fig. 16. Typically, chirality leads to a breaking of inversion symmetry. The dynamically imposed chirality shows the same features. The effect we observe for SWs is somewhat similar to the phenomenon observed in the context of non-Hermitian optics [26] (in fact, for narrow waveguides in the paraxial approximation, our models can be mapped to the PT-symmetric model used for coupled photonic waveguides [26]), and allows us to switch the propagation of MSSWs on and off in a selected layer.

VII. DESIGN OF A SPIN-WAVE DIRECTIONAL COUPLER

The functionality of a reconfigurable nanoscale spin-wave directional coupler depends on the structure of the band gap (efficiently controlled through an electric field) and the direction of the ground-state equilibrium magnetization. The direction of the magnetization can be switched via an external magnetic field or a current-induced spin-orbit torque (SOT). The SOT has in addition certain advantages; see Ref. [27] for more details.
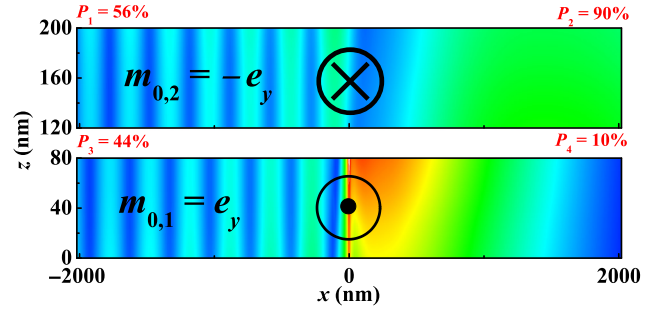

FIG. 19. Spatial profiles of amplitudes of propagating SWs in two antiparallel films. The SWs are excited by a rf field with frequency 3.53 GHz.

FIG. 18. Spatial profiles of amplitudes of propagating SWs in two parallel films. The SWs are excited by a rf field with frequency 3.44 GHz.
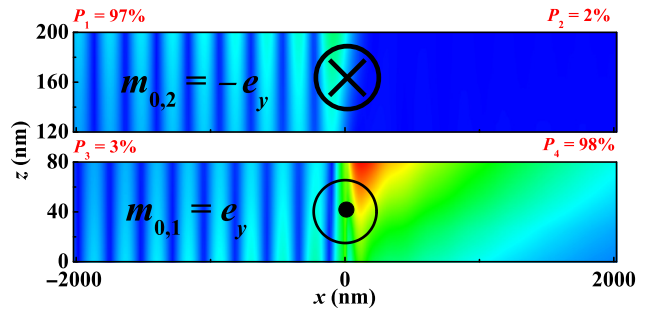

FIG. 20. Spatial profiles of amplitudes of propagating SWs in two antiparallel films. The SWs are excited by a rf field with frequency 4.24 GHz.
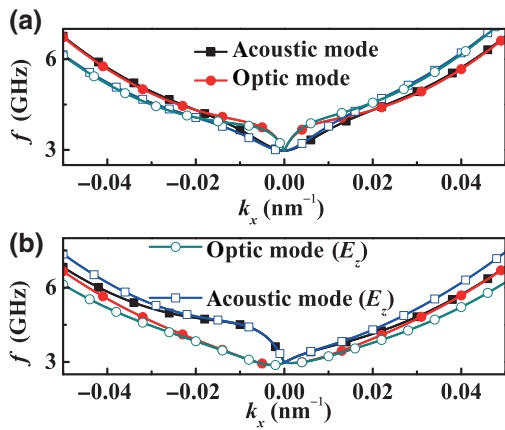
FIG. 21. Analytically derived spin-wave dispersion relations for $E_z = 0.34$ MV/cm (open circles and squares) and without electric field (solid circles and squares), in coupled parallel (a) and antiparallel (b) films.

FIG. 23. Spatial profiles of amplitudes of propagating SWs in two antiparallel films. The external electric field E_z is 0.34 MV/cm, and the frequency of the rf field is 4.24 GHz.

Here, we propose a reconfigurable directional coupler utilizing the SOT for controlling the direction of the magnetization. In parallel coupled films, the dispersion relations, as well as coupling lengths L, are the same for opposite propagation directions of MSSWs. Thus $P_1 \approx P_3$ and $P_2 \approx P_4$ reach their maxima or minima synchronously at the same moment in time, as demonstrated in Figs. 17 and 18. After switching of the magnetization distribution to the antiparallel direction, the dispersion relation and L become asymmetric (Fig. 14), and a large difference between the left-side output P_1 or P_3 and the right-side output P_2 or P_4 develops, as demonstrated in Figs. 19 and 20.

An external electric field E_z applied to both films shifts the SW dispersion [see Eqs. (7) and (8)], as demonstrated in Fig. 21. The shifting of the dispersion relations changes the value of L, leading to an electrically reconfigurable directional coupler. In Figs. 22 and 23, the output P_i is plotted for an electric field $E_z = 0.34$ MV/cm, whereas in Figs. 19 and Ref. 20 the electric field is zero, and the value of the output P_i is different.

We note that the magnetization moments in four different regions (Fig. 6) near the output terminals allow

selective individual control, and this is a definite advantage of the functionality of the proposed directional coupler. This control is achievable through the current-induced spin-orbit torque and an external magnetic field. In Figs. 24 and 25, we show the amplitudes of propagating MSSWs in antiparallel films with magnetic domain walls located near the center ($x = 0$). SWs propagating in the $+x$ and $-x$ directions share the same chirality, and thus we obtain symmetric outputs in antiparallel films, i.e., $P_1 = P_2$ and $P_3 = P_4$.

For an experimental realization, we suggest the following schemes for exciting spin waves with wave vectors up to 0.04 nm^{-1}. The emergent net ferroelectric polarization coupled (through the magnetoelectric coupling) to the external electric field mimics an effective DM term. Thus, an applied nonuniform electric field is equivalent to a nonuniform DM term and leads to a particular type of torque, termed an inhomogeneous electric torque [19]. The expression for the inhomogeneous electric torque is similar to the spin-transfer torque $l_E \mathbf{m} \times (\mathbf{m} \times \mathbf{p}_E)$. The vector $\mathbf{p}_E = \mathbf{x} \times \mathbf{e}_i$, $\mathbf{e}_{i=x,y,z}$, points in the direction of the electric field, and the electric-field gradient $\partial_x E_i$ determines the coefficient $l_E = -\gamma c_E \, \partial_x E_i/(\mu_0 M_s)$. Therefore, an applied oscillating inhomogeneous electric field $E_y = 0$ ($x < 0$) and $E_y = E_1(t)$ ($x > 0$), with $\mathbf{p_E} = \mathbf{z}$ at $x = 0$, leads to an oscillating electric torque, and excites a magnetization oscillation at $x = 0$ and short-wavelength spin
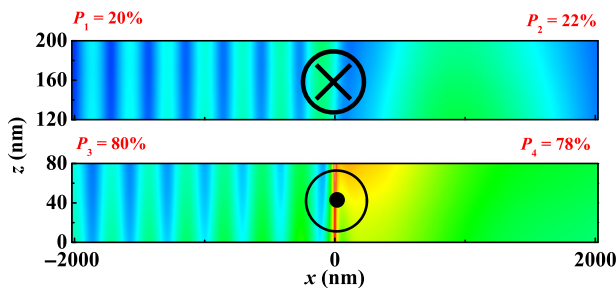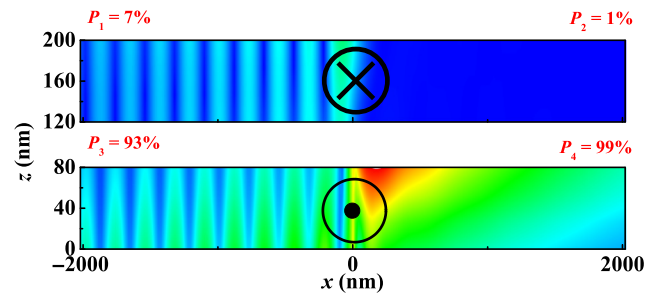

FIG. 22. Spatial profiles of amplitudes of propagating SWs in two antiparallel films. The frequency of the rf field is 3.53 GHz, and the amplitude of the external electric field E_z is 0.34 MV/cm.
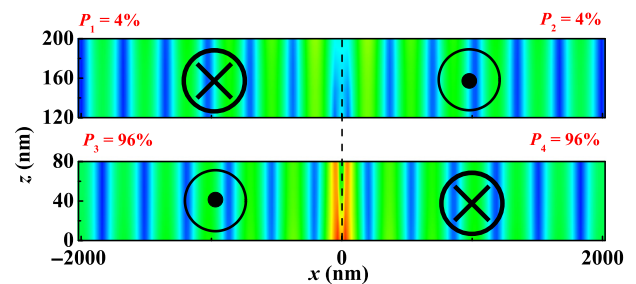

FIG. 24. Spatial profiles of amplitudes of propagating SWs in two antiparallel films with domain walls. The frequency of the rf field is 3.34 GHz.
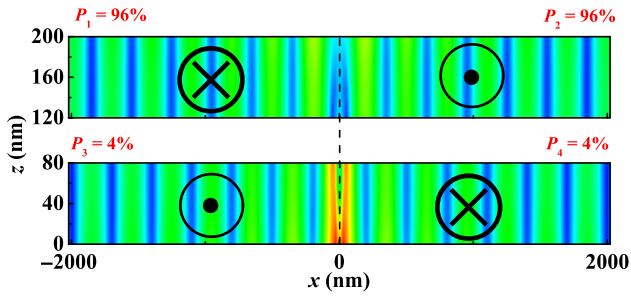
FIG. 25. Spatial profiles of amplitudes of propagating SWs in two antiparallel films with domain walls. The frequency of the rf field is 3.52 GHz.

waves. The inhomogeneous electric field can be realized by a combination of a uniform electric field and a normal-metallic cap layer shielding the region $x < 0$. Besides, via a microwave magnetic field from antennas, one can excite large-wavelength spin waves in the region of a large internal effective magnetic field. The wavelength of the wave becomes smaller as soon as the wave crosses into a region of lower internal effective magnetic field. This method was proposed in Ref. [28]. The different effective magnetic fields can be achieved by changing the geometry of the sample, by attaching an exchange-bias layer to part of the magnetic layer, or by covering the waveguide with a superconducting material (at a temperature T below T_c).

VIII. SWITCHING OF THE STATIC MAGNETIZATION

For practical realization, we suggest using the spin-Hall torque to switch the magnetization in coupled films.
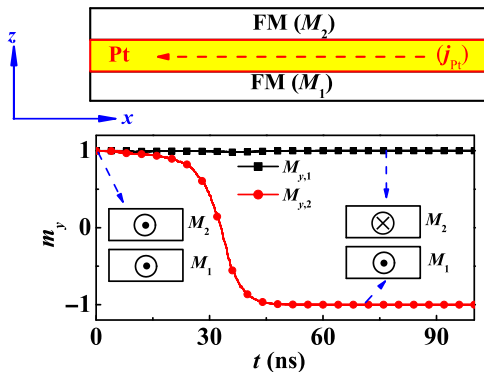

FIG. 26. Generation of the antiparallel ground state. In the schematic (upper panel), a Pt spacer is placed between two dipolarly coupled films (labeled FM). Injecting an electronic current $\mathbf{j}_{Pt}$ in the $-\mathbf{x}$ direction and applying opposite spin-Hall torques in the two films with a parallel initial state reverses the magnetization of one film ($\mathbf{M}_2$ in this figure) after tens of nanoseconds. The switching process (i.e., the time dependence of M_y) is demonstrated in the lower panel.
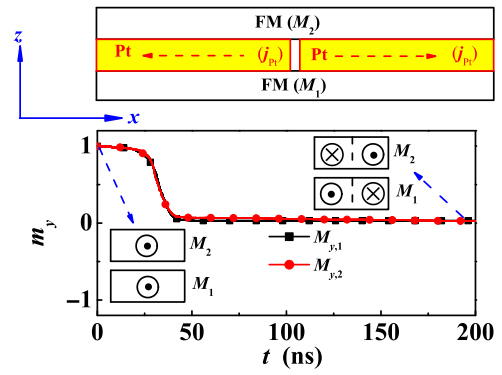

FIG. 27. Generation of the antiparallel domain-wall state. Two independent Pt spacer layers (see top panel) are embedded between two films (labeled FM). After $\mathbf{j}_{Pt}$ has been injected in different directions in the two Pt layers, the induced spin-Hall torque generates the desired domain-wall structure. The switching process (i.e., the time dependence of M_y) is demonstrated in the lower panel. The gap between the two Pt layers along the x axis is 200 nm.

As shown in Fig. 26, a Pt spacer with an electronic current $\mathbf{j}_{Pt}$ in the $-\mathbf{x}$ direction generates spin-Hall torques $\gamma c_j \mathbf{M} \times \boldsymbol{\sigma} \times \mathbf{m}$. Here, $\boldsymbol{\sigma} = \mp \mathbf{z} \times \mathbf{j}_{Pt}$ represents the polarization direction, the coefficient c_j is proportional to the electronic current density in the Pt, and $-\mathbf{z}$ and $+\mathbf{z}$ correspond to the bottom and top layers, respectively. Also, we assume a small anisotropy constant $K_y = 3500$ J/m^3 (the axis is along y) in both films. The torques have opposite directions in the two layers, and $\mathbf{M}_{1,2}$ tends to be aligned along the $\pm\mathbf{y}$ direction. For $c_j = 790$ A/m, the switching of magnetizations induced by the spin-Hall torque is shown in Fig. 26. In tens of nanoseconds, the state with parallel magnetizations is switched to the antiparallel state. After the electric current is turned off, the system stays in the antiparallel state. By applying a strong enough uniform magnetic field, one can easily switch the state back to the parallel state.

To generate the desired configuration of magnetic domain walls, we use the spin-Hall torque, as demonstrated in Fig. 27. Two Pt layers with opposite electric currents generate opposite torques in the two edges of an individual film. The torques are also opposite in different films. The spin-Hall torques obtained with $c_j = 790$ A/m generate the particular structure of domain walls studied here, e.g., that shown in Fig. 27. The magnetic domain walls are stable after the electric current is turned off.

IX. CONCLUSIONS

Magnetostatic surface waves and surface waves propagating in coupled parallel waveguides are prototype examples of the simplest integrated magnonic circuits. The surface waves, coupled through the dipole-dipole interaction, periodically exchange energy. For high fidelity of

magnonic gates, the process of energy exchange should be well under control. In the present paper, we propose a particular type of surface-wave magnonic gate controlled through an external static electric field. By varying the strength or direction of the electric field, it is possible to shift selectively the chiral MSSW dispersion relation in the coupled waveguides. This fact is used for manipulation of the propagation and transfer of SWs in waveguides. By combining these effects, we propose an electrically reconfigurable nanoscale spin-wave directional coupler, the outputs of which can be selectively changed via controlling the electric field or the magnetization. The electric field adopted is easy to realize and control, which is helpful for designing high-fidelity surface-wave magnonic devices.

[1] R. Shindou, R. Matsumoto, S. Murakami, and J. I. Ohe, Topological chiral magnonic edge mode in a magnonic crystal, Phys. Rev. B **87**, 174427 (2013).

[2] L. Zhang, J. Ren, J. S. Wang, and B. Li, Topological magnon insulator in insulating ferromagnet, Phys. Rev. B **87**, 144101 (2013).

[3] X. S. Wang, H. W. Zhang, and X. R. Wang, Topological Magnonics: A Paradigm for Spin-Wave Manipulation and Device Design, Phys. Rev. Appl. **9**, 024029 (2018).

[4] R. Chisnell, J. S. Helton, D. E. Freedman, D. K. Singh, R. I. Bewley, D. G. Nocera, and Y. S. Lee, Topological Magnon Bands in a Kagome Lattice Ferromagnet, Phys. Rev. Lett. **115**, 147201 (2015).

[5] R. Shindou, J. I. Ohe, R. Matsumoto, S. Murakami, and E. Saitoh, Chiral spin-wave edge modes in dipolar magnetic thin films, Phys. Rev. B **87**, 174402 (2013).

[6] E. Iacocca and O. Heinonen, Topologically Nontrivial Magnon Bands in Artificial Square Spin Ices with Dzyaloshinskii-Moriya Interaction, Phys. Rev. Appl. **8**, 034015 (2017).

[7] A. V. Chumak, V. I. Vasyuchka, A. A. Serga, and B. Hillebrands, Magnon spintronics, Nat. Phys. **11**, 453 (2015).

[8] K. Alexander, B. Mingqiang, and L. W. Kang, Magnonic logic circuits, J. Phys. D: Appl. Phys. **43**, 264005 (2010).

[9] S. Urazhdin, V. E. Demidov, H. Ulrichs, T. Kendziorczyk, T. Kuhn, J. Leuthold, G. Wilde, and S. O. Demokritov, Nanomagnonic devices based on the spin-transfer torque, Nat. Nanotechnol. **9**, 509 (2014).

[10] Q. Wang, P. Pirro, R. Verba, A. Slavin, B. Hillebrands, and A. V. Chumak, Reconfigurable nanoscale spin-wave directional coupler, Sci. Adv. **4**, e1701517 (2018).

[11] A. V. Sadovnikov, C. S. Davies, S. V. Grishin, V. V. Kruglyak, D. V. Romanenko, Y. P. Sharaevskii, and S. A. Nikitov, Magnonic beam splitter: The building block of parallel magnonic circuitry, Appl. Phys. Lett. **106**, 192406 (2015).

[12] X. Zhang, T. Liu, M. E. Flatte, and H. X. Tang, Electric-Field Coupling to Spin Waves in a Centrosymmetric Ferrite, Phys. Rev. Lett. **113**, 037202 (2014).

[13] T. Liu and G. Vignale, Electric Control of Spin Currents and Spin-Wave Logic, Phys. Rev. Lett. **106**, 247203 (2011).

[14] A. A. Serga, A. V. Chumak, and B. Hillebrands, YIG magnonics, J. Phys. D: Appl. Phys. **43**, 264002 (2010).

[15] M. Mohseni, R. Verba, T. Bracher, Q. Wang, D. A. Bozhko, B. Hillebrands, and P. Pirro, Backscattering-Immune Chiral Spin-Wave Modes for Protected Magnon Transport at the Nano-Scale, arXiv:1806.01554.

[16] T. An, V. I. Vasyuchka, K. Uchida, A. V. Chumak, K. Yamaguchi, K. Harii, J. Ohe, M. B. Jungfleisch, Y. Kajiwara, H. Adachi, B. Hillebrands, S. Maekawa, and E. Saitoh, Unidirectional spin-wave heat conveyer, Nat. Mater. **12**, 549 (2013).

[17] I. Lisenkov, V. Tyberkevych, A. Slavin, P. Bondarenko, B. A. Ivanov, E. Bankowski, T. Meitzler, and S. Nikitov, Spin-wave edge modes in finite arrays of dipolarly coupled magnetic nanopillars, Phys. Rev. B **90**, 104417 (2014).

[18] M. Kostylev, Non-reciprocity of dipole-exchange spin waves in thin ferromagnetic films, J. Appl. Phys. **113**, 053907 (2013).

[19] X.-g. Wang, L. Chotorlishvili, G.-h. Guo, C. L. Jia, and J. Berakdar, Thermally assisted skyrmion drag in a nonuniform electric field, Phys. Rev. B **99**, 064426 (2019).

[20] X.-g. Wang, L. Chotorlishvili, G.-h. Guo, and J. Berakdar, Electric field controlled spin waveguide phase shifter in YIG, J. Appl. Phys. **124**, 073903 (2018).

[21] R. Zivieri, L. Giovannini, and F. Nizzoli, Acoustical and optical spin modes of multilayers with ferromagnetic and antiferromagnetic coupling, Phys. Rev. B **62**, 14950 (2000).

[22] A. Konovalenko, E. Lindgren, S. S. Cherepov, V. Korenivski, and D. C. Worledge, Spin dynamics of two-coupled nanomagnets in spin-flop tunnel junctions, Phys. Rev. B **80**, 144425 (2009).

[23] M. Beleggia, S. Tandon, Y. Zhu, and M. De Graef, On the magnetostatic interactions between nanoparticles of arbitrary shape, J. Magn. Magn. Mater. **278**, 270 (2004).

[24] R. Verba, G. Melkov, V. Tiberkevich, and A. Slavin, Collective spin-wave excitations in a two-dimensional array of coupled magnetic nanodots, Phys. Rev. B **85**, 014427 (2012).

[25] K. Di, V. L. Zhang, H. S. Lim, S. C. Ng, M. H. Kuok, X. Qiu, and H. Yang, Asymmetric spin-wave dispersion due to Dzyaloshinskii-Moriya interaction in an ultrathin Pt/CoFeB film, Appl. Phys. Lett. **106**, 052403 (2015).; J.-H. Moon, S.-M. Seo, K.-J. Lee, K.-W. Kim, J. Ryu, H.-W. Lee, R. D. McMichael, M. D. Stiles, Spin-wave propagation in the presence of interfacial Dzyaloshinskii-Moriya interaction, Phys. Rev. B **88**, 184404 (2013).

[26] C. E. Rüter, K. G. Makris, R. El-Ganainy, D. N. Christodoulides, M. Segev, and D. Kip, Observation of parity–time symmetry in optics, Nat. Phys. **6**, 192 (2010).

[27] Z. Ren, S. Liu, L. Jin, T. Wen, Y. Liao, X. Tang, H. Zhang, and Z. Zhong, Reconfigurable nanoscale spin-wave directional coupler using spin-orbit torque, Sci. Rep. **9**, 7093 (2019).; L. Chotorlishvili, Z. Toklikishvili, X. G. Wang, V. K. Dugaev, J. Barnas, J. Berakdar, Influence of spin-orbit and spin-Hall effects on the spin-Seebeck current beyond linear response: A Fokker-Planck approach, Phys. Rev. B **99**, 024410 (2019).

[28] V. E. Demidov, M. P. Kostylev, K. Rott, J. Münchenberger, G. Reiss, and S. O. Demokritov, Excitation of short-wavelength spin waves in magnonic waveguides, Appl. Phys. Lett. **99**, 082507 (2011).